

# Distance-Dependent Interaction between a Single Emitter and a Single Dielectric Nanoparticle Using DNA Origami

Nicole Siegel, María Sanz-Paz,\* Javier González-Colsa, Guillermo Serrera, Fangjia Zhu, Alan M. Szalai, Karol Kołtąj, Minoru Fujii, Hiroshi Sugimoto, Pablo Albella, and Guillermo P. Acuna\*

Optical nanoantennas can manipulate light–matter interactions at the nanoscale, modifying the emission properties of nearby single photon emitters. To date, most optical antennas are based on metallic nanostructures that exhibit unmatched performance in terms of electric field enhancement but suffer from substantial ohmic losses that limit their applications. To circumvent these limitations, there is a growing interest in alternative materials. In particular, high-refractive-index dielectrics have emerged as promising candidates, offering negligible ohmic losses, and supporting both electric and magnetic resonances in the visible and near-infrared range that can unlock novel effects. Currently, the few available studies on dielectric nanoantennas focus on ensemble measurements. Here, the DNA origami technique is exploited to study the interaction between silicon nanoparticles and organic fluorophores at the single-molecule level, in controlled geometries and at different spectral ranges within the visible spectrum. Their distance-dependent interaction is characterized in terms of fluorescence intensity and lifetime, revealing a significant modification of the decay rate together with minimal quenching and a high-fluorescence quantum yield even at short distances from the dielectric nanoparticle. This work demonstrates the advantages of dielectric nanoantennas over their metallic counterparts and paves the way for their applications in single-molecule spectroscopy and sensing.

## 1. Introduction

Optical antennas mediate and enhance interactions between light and fluorescent emitters by modifying their local electromagnetic environment.<sup>[1,2]</sup> They can focus light beyond the diffraction limit by coupling free-space propagating light into highly enhanced and localized near-fields, thus increasing the excitation rate of nearby emitters.<sup>[3]</sup> Optical antennas can also tailor the emission properties of fluorescent sources through the manipulation of the local density of states (LDOS).<sup>[4,5]</sup> To date, the majority of the studies have focused on plasmonic optical antennas based on gold or silver nanostructures. With these metallic antennas, several effects were demonstrated. Among them are the acceleration of the decay rates of fluorescent emitters<sup>[6]</sup> leading to giant luminescence enhancement,<sup>[3,7,8]</sup> ultrafast emission,<sup>[9,10]</sup> increased photostability,<sup>[11,12]</sup> and control of the emission pattern.<sup>[13–15]</sup> Despite all these advances, metals suffer from high ohmic losses throughout the visible range, which can lead

N. Siegel, M. Sanz-Paz, F. Zhu, K. Kołtąj, G. P. Acuna  
Department of Physics  
University of Fribourg  
Chemin du Musée 3, CH-1700 Fribourg, Switzerland  
E-mail: maria.sanz-paz@insp.upmc.fr; guillermo.acuna@unifr.ch


M. Sanz-Paz  
Sorbonne Université, CNRS  
Institut des NanoSciences de Paris  
INSP  
F-75005 Paris, France

J. González-Colsa, G. Serrera, P. Albella  
Group of Optics  
Department of Applied Physics  
University of Cantabria  
39005 Santander, Spain

A. M. Szalai  
Centro de Investigaciones en Bionanociencias (CIBION)  
Consejo Nacional de Investigaciones Científicas y Técnicas (CONICET)  
Godoy Cruz 2390, Ciudad Autónoma de Buenos Aires C1425FQD,  
Argentina

M. Fujii, H. Sugimoto  
Department of Electrical and Electronic Engineering  
Graduate School of Engineering  
Kobe University  
Kobe 657-8501, Japan

G. P. Acuna  
Swiss National Center for Competence in Research (NCCR) Bio-inspired  
Materials  
University of Fribourg  
Chemin des Verdiers 4, CH-1700 Fribourg, Switzerland

 The ORCID identification number(s) for the author(s) of this article can be found under <https://doi.org/10.1002/ssstr.202500299>.

© 2025 The Author(s). Small Structures published by Wiley-VCH GmbH. This is an open access article under the terms of the Creative Commons Attribution License, which permits use, distribution and reproduction in any medium, provided the original work is properly cited.

DOI: 10.1002/ssstr.202500299

to severe quenching of the fluorescence emission,<sup>[16–18]</sup> an effect that intensifies at short distances.<sup>[18]</sup>

Recently, high-refractive-index dielectric nanoparticles (HRID NPs), based on materials such as silicon, germanium or gallium phosphide, have been identified as promising alternatives to metals. One central advantage is their ability to support Mie resonances in the optical range with weaker ohmic losses in the visible spectrum.<sup>[19,20]</sup> Although they exhibit more modest electric field enhancements than gold or silver optical antennas,<sup>[19,21]</sup> the absence of losses means that emitters in close proximity to HRID NPs will not suffer from quenching and could achieve a comparable overall fluorescence. In fact, the mechanism by which these NPs affect the decay rates can be understood in terms of the Purcell factor, proportional to the mode Q factor over its volume. For Mie resonators, it has been shown<sup>[22]</sup> that the modal volumes of electric resonances are relatively low, greatly contributing to the Purcell factor and thus to the decay rates.

In addition, a key difference with metallic nanostructures lies in the fact that HRID NPs can support both electric and magnetic resonances,<sup>[21,23]</sup> which can give rise to a plethora of effects. These include directional scattering<sup>[24]</sup> and directional fluorescence emission,<sup>[25–27]</sup> the modification of the transition rates of electric and magnetic emitters<sup>[21,28–31]</sup> and the formation of super-chiral fields<sup>[32,33]</sup> for sensing applications.

To date, experiments on HRID optical antennas and their effect on nearby emitters have shown promising results in terms of fluorescence enhancement,<sup>[34–37]</sup> lower heating,<sup>[38]</sup> modification of decay rates<sup>[30]</sup> and reduced non-radiative quenching.<sup>[38,39]</sup> These results were obtained from ensemble measurements<sup>[36,38]</sup> or from diffusing molecules<sup>[34]</sup> where the distance to the antenna could not be controlled. Attempts to circumvent these limitations included the use of spacer layers<sup>[39]</sup> or scanning-probe microscopy,<sup>[30]</sup> however, with no stoichiometric control as an ensemble of emitters was addressed. In addition, it is worth mentioning that all these experiments were carried out with nanostructures obtained either by laser ablation or through the evaporation of the HRID materials. These synthesis approaches typically produce amorphous or polydisperse nanostructures with a larger imaginary part of their refractive index hindering its reproducibility.<sup>[40,41]</sup> Therefore, despite the extensively predicted potential of HRID materials to advance the field of optical antennas,<sup>[20,25,42,43]</sup> an experimental study of the interaction between HRID NPs and single fluorescent emitters at the single-molecule level with nanometer precision and stoichiometric control is still missing.

Here, we use the DNA origami technique<sup>[44]</sup> to place individual organic fluorophores and colloidal silicon nanoparticles<sup>[45]</sup> (SiNPs) with nanometric precision. By varying their interdistances and controlling the geometry, we can study their interaction at the single-molecule level. Furthermore, the SiNPs employed in this work are both crystalline and monodispersed. Therefore, they exhibit a much lower imaginary part in the dielectric permittivity throughout the visible range compared to the amorphous Si nanostructures commonly used in lithography, potentially leading to lower non-radiative losses.<sup>[30,34]</sup> We carry out fluorescence intensity and lifetime measurements in two different spectral ranges that correspond to fractions of the spectrum where either the SiNP's electric or magnetic dipolar mode prevails. Our results show for both spectral ranges that, while the radiative decay is enhanced close to the NP's surface, the non-radiative

rate remains essentially unaltered at values smaller than the radiative decay rate. This contrasts with the behavior observed for metallic nanoparticles,<sup>[18]</sup> and emphasizes the advantage of using dielectric materials for nanophotonic applications without the need to resort to different approaches to avoid quenching.<sup>[46,47]</sup> Finally, our results are supported by numerical simulations, which show good agreement with the experimental data, evidencing the outstanding positioning control enabled by the DNA origami technique for placing SiNPs.

## 2. Experimental Results

**Figure 1A** depicts a schematic representation of the DNA origami employed. It consists of a two-layer 12-helix rectangular structure with dimensions of  $\approx 180 \times 20 \times 5$  nm (length  $\times$  width  $\times$  height) and a “mast” in the center<sup>[48]</sup> (see further details about the DNA origami design in Table S4 and S5, Supporting Information). The DNA origami design includes 6 biotinylated modifications on the bottom side for their immobilization onto glass coverslips functionalized with neutravidin. Furthermore, the design also includes 32 binding sites consisting of a mixture of A<sub>8</sub> and A<sub>18</sub> single-stranded (ss) DNA handles to accommodate a single SiNP at the upper side (Figure 1A). Finally, a single organic fluorophore pair consisting of an ATTO 542 and an ATTO 647 N, was incorporated.

In total, three different DNA origami structures were prepared (Figure 1B), which differed only in the position of the fluorophore pair, covering an estimated distance to the SiNP's surface of  $\approx 7$ , 20, and 80 nm. The crystalline and monodispersed colloidal SiNPs<sup>[49]</sup> employed had a diameter of  $(140 \pm 8)$  nm (see Figure 1C and details in the supporting information). For this size, SiNPs exhibit in water Mie resonances within the visible spectrum, as shown in the numerical simulations of the scattering cross section and mode decomposition in Figure 1D. This highlights the broadband behavior of SiNPs. Considering the two dyes used in this work, we expect a higher effect of the SiNP on the ATTO 542 as compared to the ATTO 647 N due to a higher overlap (see Figure 1D).

The incorporation of the SiNPs to the DNA origami structures was performed following a “surface synthesis” approach.<sup>[18]</sup> To do so, first the DNA origami were immobilized onto glass coverslips through the biotin-neutravidin interaction. Second, a solution containing the previously DNA-functionalized SiNPs was added (see Figure 1A). After incubation, the solution containing the SiNPs was removed. We chose this approach over the “solution synthesis”<sup>[15]</sup> method since by adjusting the incubation time and NP concentration, the ratio of DNA origami hybridized with a single SiNP or none can be manipulated. This can be exploited to have a control reference population within the same sample that is being measured, which will be identified by subsequent colocalization with scanning electron microscopy (SEM). In addition, the surface synthesis approach yields a more consistent alignment of the SiNP and the fluorophore pair with respect to the incident light direction. In this way, dyes are located in the plane below the SiNP, so that effects such as the enhancement of the excitation field can be neglected (see simulations of the excitation electric field enhancement in Figure S1, Supporting Information). To verify proper assembly and to estimate the incorporation yield, we first performed fluorescence

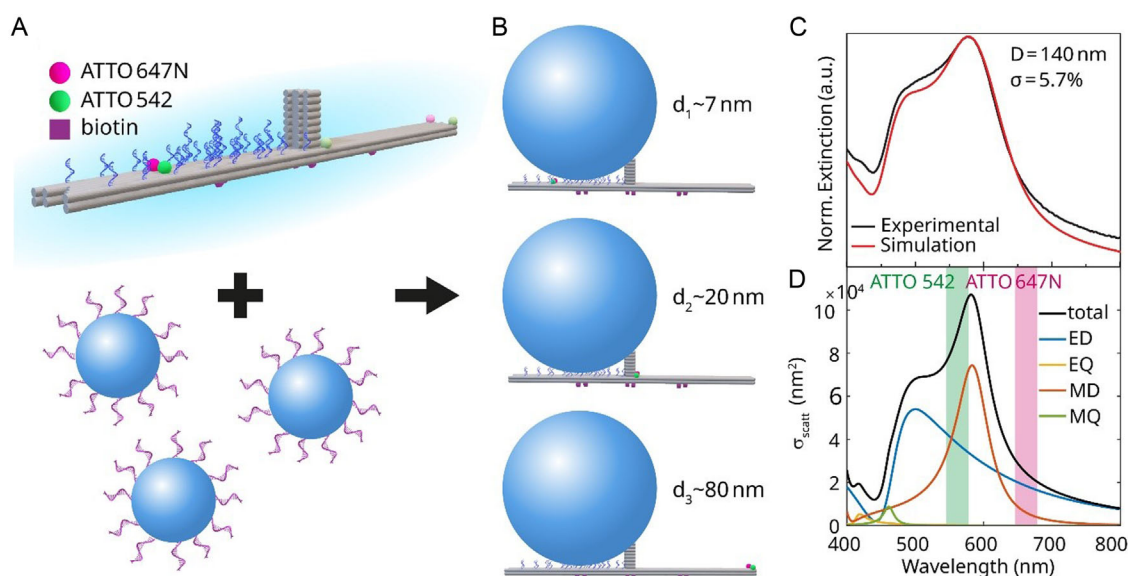


**Figure 1.** Monomer assembly using DNA origami and SiNPs. A) Sketch of the DNA origami used, displaying the different dye-NP distances (magenta and green dots) studied and the polyadenine (blue protrusions) strands to attach subsequently added DNA-functionalized SiNPs. Biotin molecules (violet diamonds) on the bottom of the origami are used for binding to the surface of a functionalized glass slide. B) Illustration of the assembled monomer antennas for the three different dye-NP distances used ( $d_1$ ,  $d_2$ , and  $d_3$ ). C) The extinction spectrum from a solution of SiNPs is measured (black) and compared to simulations (red). From these simulations, the average diameter  $\bar{D}$  and the polydispersity  $\sigma/\bar{D}$  of the NP distribution are obtained. D) Scattering cross-section and mode decomposition for a SiNP of 70 nm radius in water. The shaded areas highlight the spectral emission bands of the two dyes used in our experiments (ATTO 542 in green and ATTO 647 N in magenta).

lifetime imaging microscopy (FLIM) on the DNA origami sample with the fluorescent pair located at distance  $d_1$  (Figure 2A). The results for the ATTO 647 N dye show two distinct populations with lifetimes of around 4 ns, in agreement with the intrinsic lifetime of the dye, and shorter lifetimes of  $\approx 2.5$  ns. These images were colocalized with the positions of the SiNPs as determined via SEM imaging (Figure 2B) of the same area. The overlay of both images (Figure 2C) reveals no aggregation of SiNPs, minor non-specific binding of NPs to the surface, and a significant fraction of the DNA origami containing no NP ( $\approx 25\%$ ). Moreover, it shows that the lifetime reduction can be ascribed to the incorporation of a single SiNP into the DNA origami—

therefore, spots colocalizing with a single SiNP were used for further analysis, and the ones without NP were taken as a reference.

To investigate the effect of a SiNP on the emission rates of a single dye, we extracted the fluorescence intensity and lifetime of individual dye-SiNP constructs. The results for the ATTO 647 N at distances  $d_1$ ,  $d_2$ , and  $d_3$  are included in Figure 3A–C, respectively, whereas the corresponding results for the ATTO 542 are included in Figure 3D–F. The reported fluorescence intensity is normalized to the average fluorescence intensity of the reference population, whereas for the fluorescence lifetime we used the absolute value since it is less prone to deviations due to

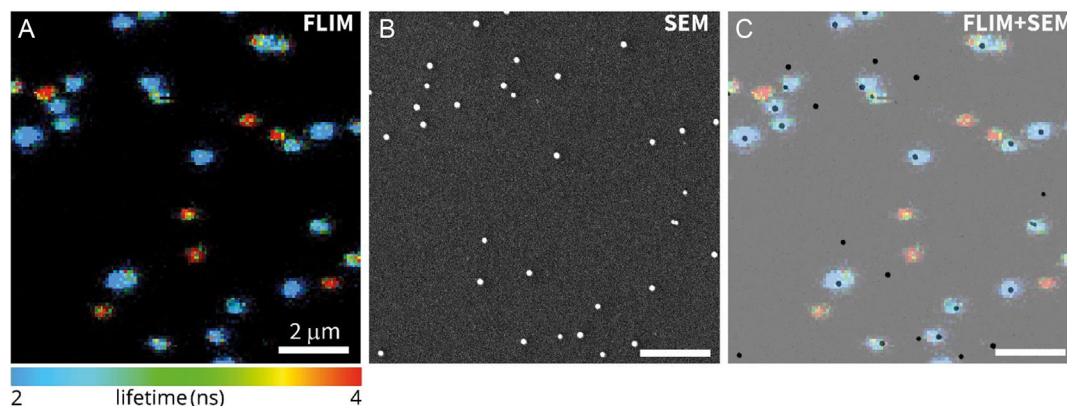


**Figure 2.** Monomer imaging and colocalization. A) Fluorescence lifetime image from ATTO 647 N at  $d_1$  and B) corresponding SEM image of a region showing colocalization between fluorescent spots and SiNPs, C) overlay between both. Scale bars: 2  $\mu\text{m}$ .

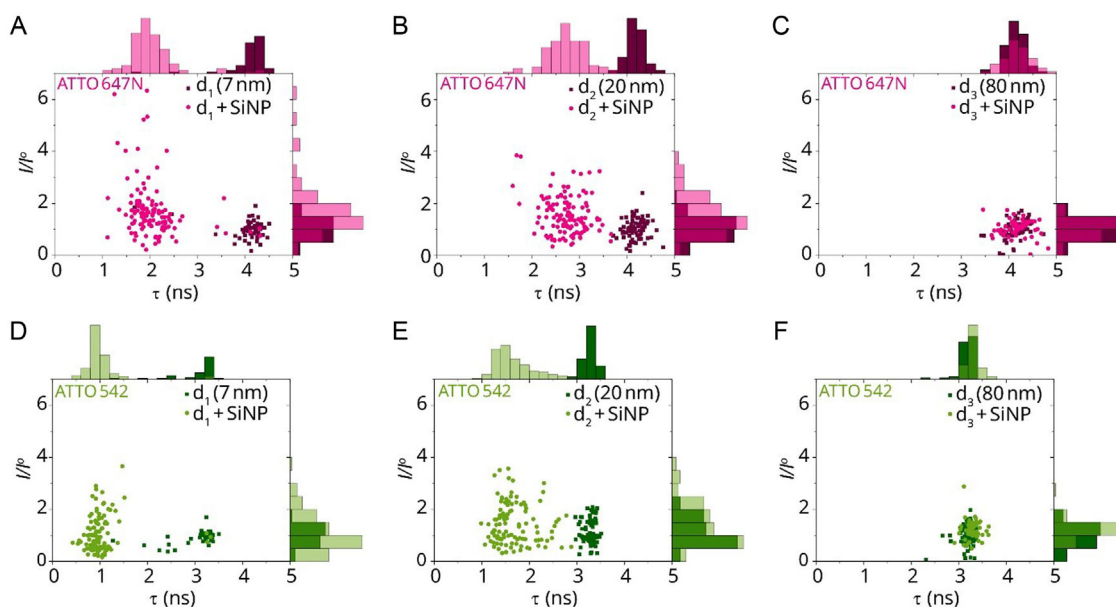


**Figure 3.** Broadband lifetime reduction close to SiNPs. Intensity enhancement  $I/I^0$  versus lifetime  $\tau$  for the two dyes present in our DNA origami construct: A–C) ATTO 647 N and D–F) ATTO 542, located at various distances ( $d_1 \approx 7$  nm,  $d_2 \approx 20$  nm,  $d_3 \approx 80$  nm) to the SiNP (lighter color) and in absence of the NP (darker color). Number of events measured (A)  $N_{\text{ref}} = 55$ ,  $N_{\text{Si}} = 122$ , (B)  $N_{\text{ref}} = 81$ ,  $N_{\text{Si}} = 126$ , (C)  $N_{\text{ref}} = 71$ ,  $N_{\text{Si}} = 58$ , (D)  $N_{\text{ref}} = 41$ ,  $N_{\text{Si}} = 112$ , (E)  $N_{\text{ref}} = 74$ ,  $N_{\text{Si}} = 108$ , (F)  $N_{\text{ref}} = 60$ ,  $N_{\text{Si}} = 59$ .

alignment or slight variations in laser power. As expected, the measurements on the reference population yield a rather compact distribution with similar average fluorescence lifetimes for each dye. For the dye-SiNP hybrids at distance  $d_3$ , in the green and red spectral ranges, both the fluorescence intensity and lifetime overlap with the reference values. Therefore, we conclude that at distances  $>80$  nm the interaction is negligible. The situation is different for distances  $d_1$  and  $d_2$  in which a clear deviation from the reference values can be observed for both dyes, pointing to the broadband effect of SiNPs.

To better evaluate this distance-dependent trend, we plot in **Figure 4A,B** the median relative fluorescence lifetime  $\tau/\tau^0$  and

intensity enhancement  $I/I^0$  for both dyes as a function of the distance to the NP surface. Here, the error bars represent the median absolute deviation (MAD). Note that the error bars are much larger for the intensity measurements than for the lifetime ones. This is related to the confocal measurement itself, where small drifts in focus and lateral position affect the detected intensity in a larger manner than the lifetime.

The main features of Figure 4 can be summarized in a lifetime reduction at  $d_1$  and  $d_2$  for both fluorophores, stronger for the ATTO 542 due to a higher spectral overlap, while the fluorescence intensity remains essentially unchanged regardless of the dye or position.<sup>[39]</sup> These two observations hint at the

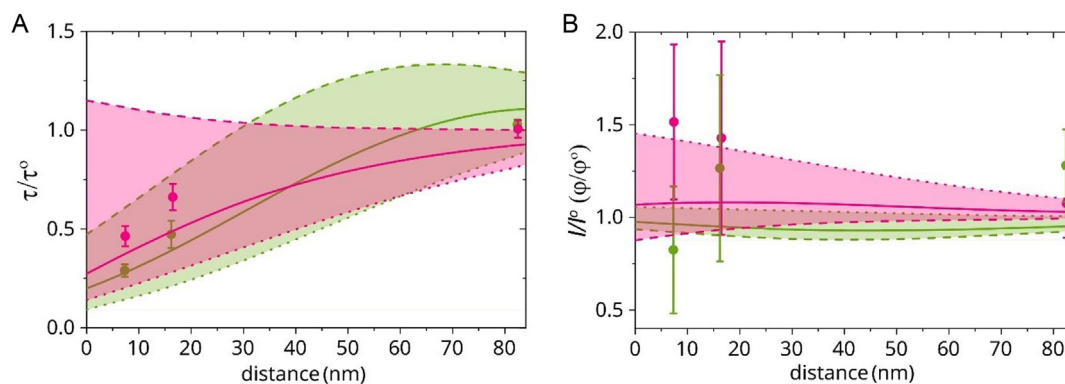


**Figure 4.** Distance-dependent lifetime and intensity changes. A) Changes in lifetime  $\tau$  and B) intensity  $I$  with respect to the isolated molecule as a function of the dye-SiNP distance for the two emitters: magenta for ATTO 647 N and green for ATTO 542. Shadowed areas indicate the range between the simulated values for radial (dotted) and tangential (dashed) orientations, and the solid line represents the trend for an average orientation. Note that simulations in (B) correspond to changes in quantum yield  $\phi$ . Experimentally obtained values of intensity changes with their corresponding error bars (dots representing the median and bars the median absolute deviation) fall well within those expected ranges.

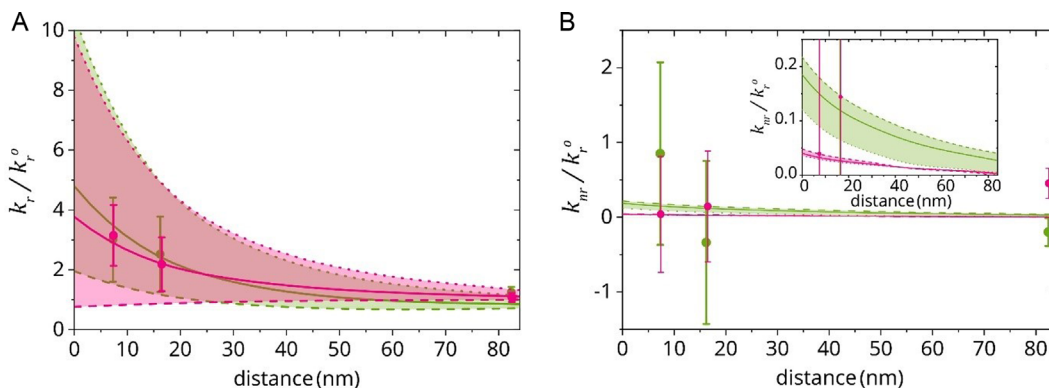


**Figure 5.** Comparison between experimentally extracted rates and simulated values. A) Changes in radiative decay rate  $k_r$  and B) non-radiative decay rate  $k_{nr}$  with respect to the isolated molecule as a function of the dye-SiNP distance for the two emitters: magenta for ATTO 647 N and green for ATTO 542. Shadowed areas indicate the range between the simulated values for radial (dotted) and tangential (dashed) orientations, and the solid line represents the trend for an average orientation. Experimentally obtained values (dots representing the median and bars the median absolute deviation) fall well within those expected ranges. Inset in (B) shows a zoom-in for better visualization of the simulated values.

conclusion that the radiative decay rate dominates the lifetime decrease,<sup>[50]</sup> even at this short distance, as opposed to what happens with gold or silver NPs.<sup>[51]</sup>

To support this observation, we used those measured fluorescence intensity and lifetime to determine the distance-dependent modification of the decay rates for a single molecule in the vicinity of a NP and compared it to the isolated case.<sup>[17,51]</sup> First, the relative change in quantum yield  $\frac{\varphi}{\varphi^0}$  can be approximated to the relative change in intensity  $\frac{I}{I^0}$ <sup>[17]</sup>

$$\frac{I}{I^0} = \frac{\varphi}{\varphi^0} = \frac{k_{exc} \eta}{k_{exc}^0 \eta^0} \rightarrow \frac{\varphi}{\varphi^0} = \frac{I}{I^0} \frac{k_{exc}^0 \eta^0}{k_{exc} \eta} \approx \frac{I}{I^0} \quad (1)$$

where the superscript  $x^0$  corresponds to the reference case (isolated dye without NP),  $k_{exc}$  refers to the excitation rate (which is proportional to the local electric field intensity), and  $\eta$  is the collection efficiency. In Equation (1), we have neglected changes in the overall product of  $\frac{k_{exc}^0 \eta^0}{k_{exc} \eta}$  as expected for the geometry of the hybrid system with the dye located in the polar plane. However, a thorough analysis to account for these effects can be found in Figure S1 and S2, Supporting Information. Then, using this change in quantum yield together with the measured lifetimes ( $\tau^0$  and  $\tau$ ) and the intrinsic quantum yield  $\varphi^0$  of the commercial dyes employed, the changes in decay rates can be obtained from

$$\frac{k_r}{k_r^0} = \frac{\varphi}{\varphi^0} \frac{\tau^0}{\tau} \quad (2)$$

$$\frac{k_{nr}}{k_r^0} = \left( \frac{1}{\varphi^0} - \frac{\varphi}{\varphi^0} \right) \frac{\tau^0}{\tau} \quad (3)$$

with  $k_r$  and  $k_{nr}$  the radiative and non-radiative decay rates, respectively. These rates are estimated for both dyes at the three different distances, and the resulting values are shown in **Figure 5** (median and error bars in green for ATTO 542 and magenta for ATTO 647 N). For the two different spectral ranges sampled,  $k_r$  increases closer to the SiNP surface (Figure 5A), reaching enhancement values close to 3. In contrast,  $k_{nr}$  remains essentially independent of the distance to the SiNP with lower enhancement values  $< 1$  (Figure 5B). The uncertainty in the determination of  $k_{nr}$  is higher

than that of  $k_r$  as expected from the subtraction in Equation (3). In conclusion, changes in  $k_r$  dominate the lifetime reduction even at short distances, as they are comparable or even one magnitude larger than changes in  $k_{nr}$ , that is,  $\frac{k_r}{k_{nr}} > 3$  (Figure 5B). This is radically different from what has been measured for gold, where the non-radiative rate surpasses the radiative one by one order of magnitude ( $\frac{k_r}{k_{nr}} \approx 0.1$ ).<sup>[51]</sup> Overall, this makes a  $>30$ -fold improvement of HRIDs over plasmonic materials for enhancing  $k_r$  over  $k_{nr}$ . Despite this difference, the lifetime is still reduced around a SiNP. For the shortest distance, the lifetime is lowered on average by 2.5-fold, a reduction that is larger than previously measured values around a single NP.<sup>[36,39]</sup>

The experimental results are compared to numerical simulations performed for the two orientations of the fluorophore's transition dipole moment (radial or tangential to the SiNP surface). These simulations are included in Figure 4 and 5, where dotted (dashed) lines represent the case of the radial (tangential) orientation, and the solid lines represent a weighted average ( $1 \times$  radial +  $2 \times$  tangential). Since our measurements are carried out in an aqueous solution, dyes can be either freely rotating or fixed at any random orientation. Thus, the experimentally extracted rates are expected to fall in between those two extreme cases (shadowed areas in Figure 4 and 5). Indeed, we observe a good agreement with the simulations for the different parameters. The simulations also reveal, as opposed to the case of gold,<sup>[51]</sup> the low sensitivity of the non-radiative rate to the emitter orientation (Figure 5B).<sup>[52]</sup> Note that changes in the collection efficiency or the excitation rate due to the SiNP itself have been neglected in Figure 5, that is,  $\frac{k_{exc}^0 \eta^0}{k_{exc} \eta} = 1$ . A more detailed analysis taking into account those changes, has been included in Figure S3, Supporting Information and shows that our conclusions remain unaltered with values that show good agreement with the simulations.

### 3. Conclusion

In conclusion, we have experimentally proven the effectiveness of silicon as an alternative to plasmonic materials for optical

antennas. This was evidenced by the absence of fluorescence quenching of emitters at short distances to single SiNPs for two different spectral ranges within the visible regime. We have also extracted the changes in radiative and non-radiative decay rates from measured fluorescence intensity and lifetime values as a function of the distance to the SiNP. Our results show that changes in lifetime are dominated by an enhanced radiative decay rate, which can reach an order of magnitude more than changes in the non-radiative one. This opposes the established behavior for metals, where losses are the main source of decay at shorter distances to the NP. Such reduced quenching eliminates the need of spacer layers commonly used for sensing, opening promising possibilities for the use of high-refractive-index materials in the field.

The results obtained are also rationalized through numerical simulations that exhibit a good agreement with the values of  $\varphi/\varphi^0$ ,  $\tau/\tau^0$ ,  $\frac{k_r}{k_r^0}$ , and  $\frac{k_{nr}}{k_{nr}^0}$  retrieved. This highlights the accuracy in distance control enabled by the DNA origami technique not only for metallic NPs, as it has been extensively shown, but also for high-refractive-index dielectric NPs.

These findings push forward new possibilities for designing nanophotonic platforms that preserve or even enhance fluorescence emission without introducing significant non-radiative losses. In particular, the use of dielectric nanoantennas that minimize quenching could be exploited in applications such as single-molecule detection, bio-imaging, or quantum light sources,<sup>[53]</sup> where the efficiency and photostability of the emitter are critical. Furthermore, these results suggest that dielectric nanoantennas can serve as ideal photonic interfaces for fluorescent emitters, preserving their quantum efficiency while enabling strong and controlled light–matter interactions. This is particularly advantageous for their integration into photonic circuits, where maintaining emitter performance near nanostructures is essential for efficient light routing,<sup>[27]</sup> quantum photon sources, and fluorescence-based biosensors.

## 4. Experimental Section

**DNA Functionalization of SiNPs:** Crystalline SiNPs were synthesized following established protocols<sup>[49]</sup> and size-separated using a sucrose gradient centrifugation process. Initially, a gradient forming system from Biocomp was employed to mix 50 wt% sucrose (placed at the bottom) and 20 wt% (placed at the top) using a SW40 rotor at 30 rpm, with a 12-second stop between rotations. The SiNP solution (0.5 wt% in methanol) was then carefully deposited on top, ensuring that the pipette tip made contact with the gradient surface to avoid breaking surface tension. The samples were centrifuged at 2000 rcf for 90 min. Size-separated SiNP solutions were retrieved using an automated piston that gradually descended from top to bottom at a rate of 0.5 mm sec<sup>−1</sup>, collecting fractions every 3 mm. The solution was washed by centrifugation and resuspension twice with water and twice with methanol. Subsequently, SiNPs 0.04 wt% (diameter = 141 nm with SD ≈ 15 nm as calculated from the extinction simulated spectra, see supporting information) were dispersed in anhydrous DMF (10 mL) by ultrasonication, followed by the addition of CPTMS with a ratio of 200 CPTMS molecules per nm<sup>2</sup> of NPs. After 2 h of sonication at 70 °C, NaN<sub>3</sub> was added in excess, and the mixture was stirred overnight at 40 °C. The NPs were then purified by centrifugation at 2000 rcf for 10 min, followed by consecutive redispersion twice in methanol and twice in water.<sup>[54]</sup> Finally, freezing-assisted SPAAC was employed for DNA conjugation. Shortly, SiNPs (1 mL, 0.1 wt%) were centrifuged at 2000 rcf for 10 min and resuspended in a 3:1 mixture of DBCO-modified T18 and T36 (300 μL, 100 μM,

Biomers GmbH). Subsequently, 1 mL of PBS-SDS-Tween20 buffer (1X PBS pH 7.5, 0.1% SDS, 0.1% Tween20) was added to the mixture, which was then frozen at −20 °C for 2 h. The NPs were thawed by sonication for 5 min, centrifuged twice for 10 min at 2000 rcf, and resuspended in water. For further purification and size separation, a 0.5 wt% agarose electrophoresis gel (LE Agarose, Biozym Scientific GmbH) in 0.5x TAE (20 mM Tris, 5 mM Acetate, 0.5 mM EDTA) and 6 mM MgCl<sub>2</sub> was run for 3 h at 100 V. The NPs were recovered by extracting the desired band (green band corresponding to 140 nm) from the gel.<sup>[45]</sup> The extinction spectra of the NPs was measured, and the size was calculated (diameter = 140 nm with SD ≈ 8 nm as calculated from the extinction simulated spectra, see Figure 1C).

**DNA Origami Synthesis:** The DNA origami employed in this study was designed using CaDNAo,<sup>[55]</sup> and the structure files are available at <https://nanobase.org/structure/146>.<sup>[56]</sup> A 7249-nucleotide-long scaffold extracted from the M13mp18 bacteriophage (Bayou Biolabs LLC) was folded into the desired shape using 243 staples in 1xTAE (40 mM Tris, 10 mM Acetate, 1 mM EDTA), 12 mM MgCl<sub>2</sub>, pH 8 buffer. It was mixed in a 10-fold excess of staples (purchased from IDT) over scaffold, and 100-fold for the functional staples (fluorophores, biotin, and handles, purchased from Biomers GmbH) shown in Table S3 and S4, Supporting Information. The mixture was heated to 70 °C and cooled down at a rate of 1 °C every 20 min up to 25 °C. The DNA origami structures were later purified by 1% agarose (LE Agarose, Biozym Scientific GmbH) gel electrophoresis at 70 V for 2 h and stored at 4 °C.<sup>[57]</sup>

**On-Surface Assembly of Optical Nanoantennas:** Glass slides with custom-made chromium grids were cleaned through a series of sonication baths, using the following solvents in sequence: 15 min in acetone, 15 min in isopropanol, 15 min in potassium hydroxide (3 M), and 15 min in water. The surfaces were then activated by exposure to UV-ozone cleaning and subsequently coated with BSA-Biotin and Neutravidin (BSA-biotin and neutravidin, 0.5 mg mL<sup>−1</sup> in PBS), each incubated on the grid for 25 min. The DNA origami (30 pM) was incubated on the surface for 15 min, and attached via Biotin protrusions from the bottom of the structure. Finally, 2 pM of functionalized SiNPs in PBS-SDS-Tween20 buffer (1X PBS pH 7.5, 0.1% SDS, 0.1% Tween20) were incubated overnight.

**Simulation of the Decay Rates:** The simulations included in Figure 4 and 5 were performed using Lumerical FDTD together with the formalism described by Ringler et al.<sup>[58]</sup> We simulated a SiNP of 140 nm in diameter. The complex dielectric permittivity of Si was taken from Palik,<sup>[59]</sup> fitted with 3 polynomial coefficients, zero tolerance and an imaginary weight of 0.5. Background refractive index was set to 1.33 (water). The considered simulation region was 640 nm in size for all dimensions (x, y, z), and set with standard PML boundary conditions (BCs). 64 PML layers were employed for a better convergence. The simulation was set with a time of 1000 fs and an auto-shutoff level of 10<sup>−8</sup>. Symmetric BCs were used whenever possible.

Although fluorescence is a quantum mechanical effect, the radiative features of a fluorescent quantum emitter allow us to consider a classical approach. In this approximation, the emitter acts as a point-like dipole with a time-dependent dipole moment.<sup>[60]</sup> Therefore, we used a dipole source in two different contexts: a homogeneous medium with a water-like refractive index, and a non-homogeneous environment where the overall emission is affected by the presence of a dielectric nanoparticle immersed again in a water-like medium. In this case, the dipole source was placed above the NP in the z axis, at the effective distance  $d_i$  between the fluorophore and the NP's center. This configuration allows for more efficient calculations with an equivalent configuration to the experimental situation. In this configuration, and due to the NP's symmetry, a dipole oriented along the x axis yields the same result as a dipole oriented along the y axis (both perpendicular to the NP). This means that two calculations were made for the orientational average: one dipole oriented along the x axis (tangential orientation), and one oriented along the z axis (radial orientation), with the first result doubled to match the perpendicular degeneracy.

The enhancement factors of the frequency-dependent radiative  $g_r$  and non-radiative  $g_{nr}$  decay rates can be calculated from the far-field radiative  $P_r$  and absorbed  $P_{abs}$  powers,<sup>[60]</sup> respectively, and normalized to the radiated power  $P_0$  of the dipole

$$g_r(\omega) = \frac{P_r(\omega)}{P_0(\omega)} \quad (4)$$

$$g_{nr}(\omega) = \frac{P_{abs}(\omega)}{P_0(\omega)} \quad (5)$$

To calculate the radiative and absorbed powers, we use box monitors around the dipole, the nanoparticle, and the entire system. This allows us to independently integrate the power emitted by the dipole and the power absorbed by the nanoparticle, as well as to calculate the contribution of the whole system. It is important to note that with Lumerical FDTD the absolute decay rates cannot be calculated but only the relative ones. Furthermore, our computational model cannot calculate the intrinsic non-radiative decay rate since this decay includes non-radiative transitions coming from other phenomena, such as phonon excitations.

To ensure the adequacy of our simulations, we pay special attention to the mesh features, given the proposed dipole-particle distances. We select a minimum mesh step of 0.25 nm, which also allows for the correct reproduction of the nanoparticle curvature, preventing lightning rod effects. A general mesh of 2.5 nm (in all directions) was set around the NP-dipole system, while a finer 0.5 nm mesh was set in the vicinity (5 nm) of the dipole source.

As for the decay rate calculations, the total radiative  $k_r$  and non-radiative  $k_{nr}$  rates are given by the integrals

$$\frac{k_r}{k_r^0} = \int_0^\infty f_0(\omega) g_r(\omega) d\omega \quad (6)$$

$$\frac{k_{nr}}{k_r^0} = \int_0^\infty f_0(\omega) g_{nr}(\omega) d\omega \quad (7)$$

where  $k_r^0$  is the radiative decay rate of the isolated molecule, and  $f_0(\omega)$  is the integral-normalized fluorescence spectrum of the isolated dye

$$f_0(\omega) = \frac{F_0(\omega)}{\int_0^\infty F_0(\omega) d\omega} \quad (8)$$

with  $F_0(\omega)$  the fluorescence spectrum as provided in the vendor's data sheet for the two dyes used here.

From those quantities, the quantum yield can be calculated as

$$\varphi = \frac{\frac{k_r}{k_r^0}}{\frac{k_r}{k_r^0} + \frac{k_{nr}}{k_r^0} + \left(\frac{1}{\varphi^0} - 1\right)} \quad (9)$$

with  $\varphi^0$  being the intrinsic quantum yield of the isolated molecule (0.65 for ATTO 647 N and 0.93 for ATTO 542).

**Simulation of the Excitation Electric Field Enhancement:** A SiNP (dielectric permittivity as previously described) of 140 nm in diameter was placed at a distance of 5 nm from a glass substrate ( $n = 1.5$ ) an immersed in water ( $n = 1.33$ ). See diagram in Figure S1A, Supporting Information. A general mesh of 2 nm was used, with a finer mesh of  $(dx, dy, dz) = (2, 2, 0.7)$  nm at the gap between the SiNP and substrate. Illumination was performed using a total field-scattered field (TFSF) source that is circularly polarized, surrounding the NP and extending into the substrate. To compute the changes in excitation intensity, a monitor was placed in the intermediate plane between the SiNP and the substrate, where the fluorophore is lying. Values of electric field intensity were computed for the three different lateral distances  $d_i$ .

**Experimental Setup:** Measurements were performed on an inverted microscope (Olympus IX71). Excitation was performed with a randomly polarized supercontinuum white light laser (FYLA SCT1000) that was spectrally filtered to a wavelength of  $(635 \pm 5)$  nm or  $(532 \pm 5)$  nm to efficiently excite the dye (ATTO 647 N or ATTO 542, respectively). A high NA objective was used (Olympus,  $100 \times$  NA = 1.4) for excitation and collection. Emitted fluorescence was spectrally split into two paths by a dichroic mirror (640DCXR, Chroma) and detected by two avalanche photodiodes (tau-SPAD, PicoQuant) with appropriate filters. The APDs and the pulsed laser are connected to a module for time-correlated single-photon counting

(MultiHarp150, PicoQuant) for recording the photon arrival times. Measurements were performed as follows. First, a confocal image of a region of the sample was recorded, and the position of the DNA origami structures was determined. For each region imaged, measurements were taken first using red excitation to ensure all ATTO 647 N dyes are bleached before moving to green excitation in order to avoid FRET between both fluorophores. Then, each structure was brought into the center of the confocal observation volume, and fluorescence transients were recorded. Only transients with single-step photobleaching were considered to guarantee that only single molecules were studied. From those transients, the average intensity before bleaching was extracted, together with the photon arrival times. Based on the latter, a decay histogram is obtained and fitted with a mono-exponential decaying function convoluted with the instrument response function (IRF) of the system to extract the fluorescence lifetime.

**Statistical Analysis:** Data shown in all figures includes all recorded fluorescence time traces showing a clear single bleaching step (no further pre-processing). After colocalization with SEM, traces were split into reference and antenna. In Figure 3, lifetime values are plotted as recorded, whereas intensity values are normalized to the median from the reference  $I^0$ . Figure 4 and 5 show the median values from those distributions, and the error bars represent the median absolute deviation (MAD). They were represented calculated using both MATLAB and OriginLab. The sample size for each case is given in the caption of Figure 3.

## Supporting Information

Supporting Information is available from the Wiley Online Library or from the author.

## Acknowledgements

N.S. and M.S.-P. contributed equally to this work. H.S.'s work is supported by JSPS KAKENHI 24K01287 and Kobe University Strategic International Collaborative Research Grant (Type B). P.A. acknowledges funding from the MOPHOSYS Project (No. PID2022-139560NB-I00) from Proyectos de Generación de Conocimiento provided by the Spanish Agencia Estatal de Investigación of the Spanish Ministry of Science and Innovation. G.S. thanks the Spanish Ministry of Education for his predoctoral contract grant (No. FPU21/02296). G.P.A. acknowledges support from the Swiss National Science Foundation (200021\_184687), (51AU40\_229330) and the National Center of Competence in Research Bio-Inspired Materials NCCR (51NF40\_182881).

## Conflict of Interest

The authors declare no conflict of interest.

## Data Availability Statement

The data that support the findings of this study are available from the corresponding author upon reasonable request.

## Keywords

DNA nanotechnology, DNA origami, dielectric nanoparticles, low-loss materials, nanophotonics, silicon, single-molecule fluorescence

Received: May 12, 2025

Revised: July 4, 2025

Published online: July 21, 2025

- [1] V. Giannini, A. I. Fernández-Domínguez, S. C. Heck, S. A. Maier, *Chem. Rev.* **2011**, *111*, 3888.
- [2] L. Novotny, N. van Hulst, *Nat. Photonics* **2011**, *5*, 83.
- [3] A. Kinkhabwala, Z. Yu, S. Fan, Y. Avlasevich, K. Müllen, W. E. Moerner, *Nat. Photonics* **2009**, *3*, 654.
- [4] P. Biagioni, J. S. Huang, B. Hecht, *Rep. Prog. Phys.* **2012**, *75*, 024402.
- [5] P. Mühlischlegel, H.-J. Eisler, O. J. F. Martin, B. Hecht, D. W. Pohl, *Science* **2005**, *308*, 1607.
- [6] P. Bharadwaj, L. Novotny, *Opt. Express* **2007**, *15*, 14266.
- [7] A. Puchkova, C. Vietz, E. Pibiri, B. Wünsch, M. Sanz Paz, G. P. Acuna, P. Tinnefeld, *Nano Lett.* **2015**, *15*, 8354.
- [8] D. Punj, M. Mivelle, S. B. Moparhi, T. S. van Zanten, H. Rigneault, N. F. van Hulst, M. F. García-Parajó, J. Wenger, *Nat. Nanotechnol.* **2013**, *8*, 512.
- [9] G. P. Acuna, F. M. Moller, P. Holzmeister, S. Beater, B. Lalkens, P. Tinnefeld, *Science* **2012**, *338*, 506.
- [10] T. B. Hoang, G. M. Akselrod, M. H. Mikkelsen, *Nano Lett.* **2016**, *16*, 270.
- [11] J. V. Pellegrotti, G. P. Acuna, A. Puchkova, P. Holzmeister, A. Gietl, B. Lalkens, F. D. Stefani, P. Tinnefeld, *Nano Lett.* **2014**, *14*, 2831.
- [12] I. Kaminska, C. Vietz, Á. Cuartero-González, P. Tinnefeld, A. I. Fernández-Domínguez, G. P. Acuna, *Nanophotonics* **2018**, *7*, 643.
- [13] A. G. Curto, G. Volpe, T. H. Taminiau, M. P. Kreuzer, R. Quidant, N. F. van Hulst, *Science* **2010**, *329*, 930.
- [14] F. Zhu, M. Sanz-Paz, A. I. Fernández-Domínguez, X. Zhuo, L. M. Liz-Marzán, F. D. Stefani, M. Pilo-Pais, G. P. Acuna, *Nano Lett.* **2022**, *22*, 6402.
- [15] K. Hübner, M. Pilo-Pais, F. Selbach, T. Liedl, P. Tinnefeld, F. D. Stefani, G. P. Acuna, *Nano Lett.* **2019**, *19*, 6629.
- [16] P. Anger, P. Bharadwaj, L. Novotny, *Phys. Rev. Lett.* **2006**, *96*, 113002.
- [17] E. Dulkeith, A. C. Morteau, T. Niedereichholz, T. A. Klar, J. Feldmann, S. A. Levi, F. C. J. M. van Veggel, D. N. Reinhoudt, M. Möller, D. I. Gittins, *Phys. Rev. Lett.* **2002**, *89*, 12.
- [18] G. P. Acuna, M. Bucher, I. H. Stein, C. Steinhauer, A. Kuzyk, P. Holzmeister, R. Schreiber, A. Moroz, F. D. Stefani, T. Liedl, F. C. Simmel, P. Tinnefeld, *ACS Nano* **2012**, *6*, 3189.
- [19] A. I. Kuznetsov, A. E. Miroshnichenko, M. L. Brongersma, Y. S. Kivshar, B. Luk'yanchuk, *Science* **2016**, *354*, 6314.
- [20] S. Bidault, M. Mivelle, N. Bonod, *J. Appl. Phys.* **2019**, *126*, 9.
- [21] P. Albella, M. A. Poyli, M. K. Schmidt, S. A. Maier, F. Moreno, J. J. Sáenz, J. Aizpurua, *J. Phys. Chem. C* **2013**, *117*, 13573.
- [22] X. Zambrana-Puyalto, N. Bonod, *Phys. Rev. B* **2015**, *91*, 195422.
- [23] R. M. Bakker, D. Permyakov, Y. F. Yu, D. Markovich, R. Paniagua-Domínguez, L. Gonzaga, A. Samusev, Y. Kivshar, B. Lukyanchuk, A. I. Kuznetsov, *Nano Lett.* **2015**, *15*, 2137.
- [24] Y. H. Fu, A. I. Kuznetsov, A. E. Miroshnichenko, Y. F. Yu, B. Luk'yanchuk, *Nat. Commun.* **2013**, *4*, 1527.
- [25] A. E. Krasnok, A. E. Miroshnichenko, P. A. Belov, Y. S. Kivshar, *Opt. Express* **2012**, *20*, 20599.
- [26] B. Rolly, B. Stout, N. Bonod, *Opt. Express* **2012**, *20*, 20376.
- [27] K. Ozawa, H. Sugimoto, D. Shima, T. Hinamoto, M. K. Habi, Y. J. Lee, S. Raza, K. Imaeda, K. Ueno, M. L. Brongersma, M. Fujii, *Cite This ACS Appl. Opt. Mater* **2025**, *3*, 375.
- [28] M. Sanz-Paz, C. Ernandes, J. U. Esparza, G. W. Burr, N. F. Van Hulst, A. Maitre, L. Aigouy, T. Gacoin, N. Bonod, M. F. Garcia-Parajo, S. Bidault, M. Mivelle, *Nano Lett.* **2018**, *18*, 3481.
- [29] M. K. Schmidt, R. Esteban, J. J. Sáenz, I. Suárez-Lacalle, S. Mackowski, J. Aizpurua, *Opt. Express* **2012**, *20*, 18609.
- [30] D. Bouchet, M. Mivelle, J. Proust, B. Gallas, I. Ozerov, M. F. Garcia-Parajo, A. Gulinatti, I. Rech, Y. De Wilde, N. Bonod, V. Krachmalnicoff, S. Bidault, *Phys. Rev. Appl.* **2016**, *6*, 1.
- [31] H. Sugimoto, M. Fujii, *ACS Photonics* **2021**, *8*, 1794.
- [32] L. A. Warning, A. R. Miandashti, L. A. McCarthy, Q. Zhang, C. F. Landes, S. Link, *ACS Nano* **2021**, *15*, 15538.
- [33] M. L. Solomon, J. Hu, M. Lawrence, A. García-Etxarri, J. A. Dionne, *ACS Photonics* **2019**, *6*, 43.
- [34] R. Regmi, J. Berthelot, P. M. Winkler, M. Mivelle, J. Proust, F. Bedu, I. Ozerov, T. Begou, J. Lumeau, H. Rigneault, M. F. García-Parajó, S. Bidault, J. Wenger, N. Bonod, *Nano Lett.* **2016**, *16*, 5143.
- [35] J. Cambiasso, G. Grinblat, Y. Li, A. Rakovich, E. Cortés, S. A. Maier, *Nano Lett.* **2017**, *17*, 1219.
- [36] M. Adachi, H. Sugimoto, Y. Nishimura, K. Morita, C. Ogino, M. Fujii, *Small* **2023**, *19*, 1.
- [37] H. Sugimoto, M. Fujii, *Adv. Opt. Mater.* **2017**, *5*, 1.
- [38] M. Caldarola, P. Albella, E. Cortés, M. Rahmani, T. Roschuk, G. Grinblat, R. F. Oulton, A. V. Bragas, S. A. Maier, *Nat. Commun.* **2015**, *6*, 1.
- [39] M. V. Zyuzin, D. G. Baranov, A. Escudero, I. Chakraborty, A. Tsyppin, E. V. Ushakova, F. Kraus, W. J. Parak, S. V. Makarov, *Sci. Rep.* **2018**, *8*, 1.
- [40] P. A. Dmitriev, S. V. Makarov, V. A. Milichko, I. S. Mukhin, A. S. Gudovskikh, A. A. Sitnikova, A. K. Samusev, A. E. Krasnok, P. A. Belov, *Nanoscale* **2016**, *8*, 5043.
- [41] D. G. Baranov, D. A. Zuev, S. I. Lepeshov, O. V. Kotov, A. E. Krasnok, A. B. Evlyukhin, B. N. Chichkov, *Optica* **2017**, *4*, 814.
- [42] A. I. Barreda, J. M. Saiz, F. González, F. Moreno, P. Albella, *AIP Adv.* **2019**, *9*, 1.
- [43] A. García-Etxarri, R. Gómez-Medina, L. S. Froufe-Pérez, C. López, L. Chantada, F. Scheffold, J. Aizpurua, M. Nieto-Vesperinas, J. J. Sáenz, *Opt. Express* **2011**, *19*, 4815.
- [44] P. W. K. Rothmund, *Nature* **2006**, *440*, 297.
- [45] N. Siegel, H. Hasebe, G. Chiarelli, D. Garoli, H. Sugimoto, M. Fujii, G. P. Acuna, K. Kołtąj, *J. Am. Chem. Soc.* **2024**, *146*, 17250.
- [46] D. Gontero, A. V. Veglia, A. G. Bracamonte, D. Boudreau, *RSC Adv.* **2017**, *7*, 10252.
- [47] Y. Jeong, Y. M. Kook, K. Lee, W. G. Koh, *Biosens. Bioelectron.* **2018**, *111*, 102.
- [48] A. K. Adamczyk, F. Zhu, D. Schäfer, Y. Kanehira, S. Kogikoski, I. Bald, S. Schlücker, K. Kołtąj, F. D. Stefani, G. P. Acuna, *ACS Photonics* **2024**, *11*, 5272.
- [49] H. Sugimoto, T. Okazaki, M. Fujii, *Adv. Opt. Mater.* **2020**, *8*, 1.
- [50] R. M. Córdova-Castro, B. van Dam, A. Lauri, S. A. Maier, R. Sapienza, Y. De Wilde, I. Izeddin, V. Krachmalnicoff, *Light Sci. Appl.* **2024**, *13*, 7.
- [51] P. Holzmeister, E. Pibiri, J. J. Schmied, T. Sen, G. P. Acuna, P. Tinnefeld, *Nat. Commun.* **2014**, *5*, 1.
- [52] P. E. Stamatopoulou, C. Tserkezis, *OSA Contin.* **2021**, *4*, 918.
- [53] H. Alhalaby, H. Zaraket, M. Principe, *Res. Optics* **2021**, *3*, 100073.
- [54] J. Chen, M. Liu, C. Chen, H. Gong, C. Gao, *ACS Appl. Mater. Interfaces* **2011**, *3*, 3215.
- [55] S. M. Douglas, A. H. Marblestone, S. Teerapittayanon, A. Vazquez, G. M. Church, W. M. Shih, *Nucleic Acids Res.* **2009**, *37*, 5001.
- [56] E. Poppleton, A. Mallya, S. Dey, J. Joseph, P. Sulc, *Nucleic Acids Res.* **2022**, *50*, D246.
- [57] C. Zaza, G. Chiarelli, L. P. Zweifel, M. Pilo-Pais, E. Sisamakias, F. Barachati, F. D. Stefani, G. P. Acuna, *Small Methods* **2023**, *7*, 2201565.
- [58] M. Ringle, A. Schwemer, M. Wunderlich, A. Nichtl, K. Kürzinger, T. A. Klar, J. Feldmann, *Phys. Rev. Lett.* **2008**, *100*, 1.
- [59] E. D. Palik, *Handbook of Optical Constants of Solids*, Academic Press, Boston **1998**.
- [60] L. Novotny, B. Hecht, *Principles of Nano-Optics*, Cambridge University Press, UK **2006**.